Bioactive Materials 6 (2021) 3049–3061

Contents lists available at ScienceDirect

Bioactive Materials

journal homepage: www.sciencedirect.com/journal/bioactive-materials

In vitro and *in vivo* antibacterial performance of Zr & O PIII magnesium alloys with high concentration of oxygen vacancies

Tao Liang [a,b], Lilan Zeng [a], Yunzhu Shi [a], Haobo Pan [a,**], Paul K. Chu [c], Kelvin W.K. Yeung [d,***], Ying Zhao [a,*]

[a] Shenzhen Institutes of Advanced Technology, Chinese Academy of Sciences, Shenzhen, 518055, China
[b] University of Chinese Academy of Sciences, Beijing, 100049, China
[c] Department of Physics, Department of Materials Science and Engineering, Department of Biomedical Engineering, City University of Hong Kong, Tat Chee Avenue, Kowloon, Hong Kong, China
[d] Department of Orthopaedics and Traumatology, The University of Hong Kong, Hong Kong, China

ARTICLE INFO

Keywords:
Magnesium alloy
Plasma immersion ion implantation
Degradation
ZrO_2
Antibacterial property

ABSTRACT

The effects of dual Zr and O plasma immersion ion implantation (Zr & O PIII) on antibacterial properties of ZK60 Mg alloys are systematically investigated. The results show that a hydrophobic, smooth, and ZrO_2-containing graded film is formed. Electrochemical assessment shows that the corrosion rate of the plasma-treated Mg alloy decreases and the decreased degradation rate is attributed to the protection rendered by the surface oxide. *In vitro* and *in vivo* antibacterial tests reveal Zr & O PIII ZK60 presents higher antibacterial rate compared to Zr PIII ZK60 and untreated control. The hydrophobic and smooth surface suppresses bacterial adhesion. High concentration of oxygen vacancies in the surface films are determined by X-ray photoelectron spectroscopy (XPS), UV–vis diffuse reflectance spectra (UV–vis DRS) and electron paramagnetic resonance (EPR) and involved in the production of reactive oxygen species (ROS). The higher level of ROS expression inhibits biofilm formation by down-regulating the expression of *icaADBC* genes but up-regulating the expression of *icaR* gene. In addition, Zr & O PIII improves cell viability and initial cell adhesion confirming good cytocompatibility. Dual Zr & O PIII is a simple and practical means to expedite clinical acceptance of biodegradable magnesium alloys.

1. Introduction

One of the most important causes of early and late orthopedic implant failure is inflammation of surrounding bone and soft tissues due to microbial contamination [1–4]. Since prevention of bacterial adhesion without the use of medication is the best way to reduce infection [5], it is desirable to develop novel antibacterial alloys or coatings on orthopedic implants to minimize colonization formation. As potential biomedical materials, magnesium alloys have attracted much attention due to the unique biodegradable properties and elastic modulus similar to that of human bone [6,7]. However, the high degradation rate of magnesium usually results in hydrogen evolution, metal dissolution and local alkalization, which are detrimental to bone healing [8,9]. Several surface modification techniques have been proposed to mitigate the degradation rate of magnesium alloys. However, most research activities have so far focused on the enhancement of the surface corrosion resistance and biocompatibility, while the anti-bacterial capability of the coated magnesium alloys is less well understood. It is because many reports have shown that magnesium alloys have excellent antibacterial properties *in vitro* [10–13] and the antibacterial properties *in vivo* and *in vitro* are generally believed to be consistent. However, Brooks et al. [14] have recently found that magnesium alloys have antimicrobial properties *in vitro* but not *in vivo* and hence, it is imperative to improve the antibacterial capability of magnesium alloys from the viewpoint of clinical implementation.

Zr and ZrO_2 are potential antibacterial materials and their antibacterial properties against Gram negative and positive microorganisms have been reported [15,16]. In particular, zirconia is known for its

Peer review under responsibility of KeAi Communications Co., Ltd.
* Corresponding author.
** Corresponding author.
*** Corresponding author.
E-mail addresses: hb.pan@siat.ac.cn (H. Pan), wkkyeung@hku.hk (K.W.K. Yeung), ying.zhao@siat.ac.cn (Y. Zhao).

https://doi.org/10.1016/j.bioactmat.2021.02.025
Received 25 December 2020; Received in revised form 5 February 2021; Accepted 17 February 2021
Available online 9 March 2021

biocompatibility, osseointegration, and periointegration and it has been adopted clinically in dentistry and dental implantology [17,18]. Zirconia is also hydrophobic, and the hydrophobic attractive forces and electrostatic interactions between surfaces and bacteria have been observed to play a key role in suppressing biofilm formation [19]. A ZrO_2 containing graded film has been developed on Mg–Ca and Mg–Sr alloys by zirconium ion implantation and oxygen plasma immersion ion implantation and the results demonstrate the positive impact on the corrosion resistance, antibacterial properties and biocompatibility [13]. However, conventional beam-line ion implantation is quite difficult for biomedical implants with a complex shape and plasma immersion ion implantation (PIII) which is a non-line-of-sight technique is more suitable. In this work, dual zirconium and oxygen PIII is performed to modify the ZK60 magnesium alloy and the antimicrobial characteristics are determined systematically.

2. Experimental details

2.1. Sample preparation and characterization

The cast ZK60 Mg alloy (6 wt% Zn and 0.5 wt% Zr) purchased from Dongguan Fei Tai Metal Co. Ltd., China was cut into pieces with dimensions of $10 \times 10 \times 2$ mm^3. They were mechanically ground by up to 2000 grit sandpaper and ultrasonically cleaned in acetone and anhydrous ethanol. The samples were subjected to zirconium PIII using the PIII instrument in City University of Hong Kong (Plasma Technology Ltd., Hong Kong) equipped with a zirconium cathodic arc source. The samples were implanted for 0.5 h at a terminal acceleration voltage of -20 kV and base pressure of 1.7×10^{-2} Pa. Afterwards, oxygen PIII was conducted on the GPI-100 ion implanter (Plasma Technology Ltd., Hong Kong). Oxygen gas was introduced at a flow rate of 30 sccm and the plasma was triggered by 1000 W radio frequency. Using a pulsed voltage of -18 kV, a pulse width of 100 μs, and a pulsing frequency of 50 Hz, oxygen PIII was conducted for 3 h.

The surface topography and roughness of the PIII samples were characterized by atomic force microscopy (AFM; MultiMode 8, Bruker, Germany). The measurement was conducted in the ScanAsyst Mode with 512 scans on a scanned area of 2 μm × 2 μm at 0.977 Hz under ambient conditions. To evaluate the wettability, static water contact angle measurements were performed using 3 μl water droplets on a full-automatic contact angle measuring system (OCA-20, Dataphysics, Germany) and the average value was calculated from three measurements. The surface hardness and elastic modulus of samples before and after PIII were determined by nano-indentation (Nano Indenter G200, Agilent Corporation, USA). The cross section of the Zr & O PIII sample was examined by transmission electron microscopy (TEM; JEM-3200FS, JEOL, Japan) equipped with energy-dispersive X-ray spectrometry (EDS; X-max^H-100TLE, Oxford, UN). Prior to TEM observation, the specimens were prepared on an ultra-high-resolution analytical Dual-Beam™ system (SCIOS, FEI, USA) equipped with an injector needle capable of depositing Pt to protect the TEM foil from possible beam induced damage by using focused ion beam technique (FIB). Afterwards, the TEM micrograph, high-resolution transmission electron microscopy (HRTEM) images, EDS maps, and selected area electron diffraction (SAED) patterns were obtained from the Zr & O PIII film at an accelerating voltage of 200 kV. X-ray photoelectron spectroscopy (XPS; PHI 1800, ULVAC-PHI, Japan) with monochromatic Al K_α irradiation was used to determine the chemical states after PIII and the sputtering rate was about 4.3 nm · min^{-1} based on a SiO_2 reference. The binding energies were referenced to the C1s line at 284.4 eV. UV–vis spectrophotometer (UV-2450, Shimadu, Japan) with an integrated spherical attachment of $BaSO_4$ as the reference standard and an electron paramagnetic resonance spectrometer (EPR; A300, Bruker, Germany) were employed to analyze the oxygen vacancies in the film.

2.2. Degradation behavior

Electrochemical tests were performed on the Chi600E electrochemical workstation using three-electrode technique to determine the degradation rate. The potential was referenced to a saturated calomel electrode (SCE) and a platinum sheet served as the counter electrode. The testing media were simulated body fluid (SBF) and tryptic soy broth (TSB; Bacto) and samples with a surface area of 10×10 mm^2 were exposed to the solutions at 37 °C. Electrochemical impedance spectroscopy (EIS) was carried out after stabilization in the solutions for 5 min from 100 kHz to 100 mHz with a 5 mV sinusoidal perturbing signal at the open-circuit potential. The Zsimpwin software was utilized to simulate the experimental data. The polarization curves were acquired by scanning the potential at a rate of 1 mV · s^{-1} from -300 to $+600$ mV following the EIS measurement. In order to further evaluate the degradation rate of the magnesium alloy, phosphate buffer solution (PBS) of 1 ml was added to each well in a 24-well plate containing the specimen and maintained at 37 °C for 6 and 12 h. At each time point, the Mg and Zr ion concentration in the solutions were determined by inductively-coupled plasma optical emission spectroscopy (ICP-OES; Optima 7000 DV, PerkinElmer, USA).

2.3. Antimicrobial assay

2.3.1. Bacteria culture

Staphylococcus aureus (*S. aureus*, ATCC 43300) was utilized to evaluate the antibacterial properties of PIII samples. The density of the bacteria cultured in the TSB medium was quantified using a microplate reader (Multiskan GO, Thermo Fisher Scientific, USA). Serial bacterial dilution was performed to obtain a final bacteria suspension of 1×10^6 CFU · ml^{-1}.

2.3.2. In vitro antibacterial evaluation

Prior to the bacterial culture, the samples were sterilized in 70% ethanol for 15 min and rinsed with PBS for three times. The *S. aureus* suspensions of 50 μl with a concentration of 10^6 CFU · ml^{-1} were dropped onto each sample in 24-well plates and incubated at 37 °C for 6 h. The suspended and non-adhered bacteria were removed gently by rinsing with PBS. The samples were evaluated by the LIVE/DEAD BacLight Viability Kit (Invitrogen) and images were obtained by fluorescence microscopy (BX53, Olympus, Japan). The samples were fixed with 2.5% glutaraldehyde for 4 h and dehydrated sequentially in a series of ethanol-water (30%, 50%, 60%, 70%, 80%, 90%, 95% and 100%) before examination by scanning electron microscopy (SEM; ZEISS SUPRA®55, Carl Zeiss, Germany). The spread plate method was adopted to determine the number of adherent living bacteria on the specimens. After culturing for 6 h, the specimens were rinsed with PBS three times to remove the planktonic bacteria and then transferred to 5 ml of PBS and vortexed to detach the sessile bacteria. The resulting solution of 100 μl were spread on an agar plate and after incubation for 24 h, the number of grown colonies was counted by the automatic colony counter (Supcre-G6R, Shineso, China).

Intracellular reactive oxygen species (ROS) production on the specimens was assessed to investigate the antibacterial mechanism. The ROS level was characterized by the 2′,7′-dichlorodihydrofluorescein diacetate (DCFH-DA; Beyotime, China) assay [20]. The stained samples were observed by fluorescent microscopy (BX53, Olympus, Japan) and the quantitative ROS level was determined on a fluorescence microplate reader (Synergy TM 4, BioTek, USA) with excitation at 488 nm and emission at 525 nm. The bacteria-associated genes were analyzed by the quantitative real-time reverse transcription polymerase chain reaction (qRT-PCR). Bacterial suspension of 100 μl were cultured on the sample in a 24-well plate at 37 °C. After 24 h, all the planktonic and adhered bacteria were harvested by sonication and vortexing. The bacteria were pelleted by centrifugation and total RNA was collected using the bacterial RNA kits (Magen). One microgram of RNA was reversed

transcribed into complementary DNA (cDNA) using Revert Aid First Strand cDNA synthesis kit (Thermo Fisher Scientific) according to the manufacturer's instruction. qRT-PCR was examined on the machine (CFX96, Biorad, USA) using SYBR Green PCR Master Mix (Applied Biosystems, USA). The relative expression level for each gene of interest was normalized to that of the internal standard gene 16s rRNA and the primers are shown in Table S1.

2.3.3. *In vivo* antibacterial evaluation

The *in vivo* experimental protocol was approved by the Animal Care and Experiment Committee of Shenzhen Institutes of Advanced Technology, Chinese Academy of Sciences. Twenty female Sprague Dawley rats with an average weight of 250 g were used to evaluate *in vivo* antibacterial ability of the Zr & O PIII implants. Prior to surgery, the rats were anesthetized by intraperitoneal injection of 4% chloral hydrate (0.5 ml/100 g). Two subcutaneous symmetrical pockets were created on both sides of the spine by blunt dissection. The Zr & O PIII and untreated samples with dimensions of $10 \times 10 \times 2$ mm^3 were implanted into each pocket. Before surgery, the samples were co-cultured with 50 μl of *S. aureus* suspension at a concentration of 10^6 CFU · ml^{-1} for 10 min. The subcutaneous pocket was additively injected with 200 μl of the 10^6 CFU · ml^{-1} *S. aureus* suspension for the subcutaneous infection model. In addition, four rats were subcutaneously implanted with sterile Zr & O PIII and untreated samples and injected with 200 μl PBS as the negative control. Finally, the wound was sutured carefully and 3 and 7 days after surgery, the rats were sacrificed to harvest the samples.

With regarding to the infection model, the harvested samples were examined by the spread plate method and SEM. To identify the number of viable bacteria adhered on the harvested samples, all the bacteria were collected, diluted and spread onto an agar plate. After incubation for 24 h, the number of grown colonies was counted by the automatic colony counter. To observe and evaluate the adhered bacteria, the harvested samples were washed gently with PBS and fixed with 2.5% glutaraldehyde. After dehydration with gradient ethanol (30%, 50%, 60%, 70%, 80%, 90%, 95% and 100%) and sputter-coating with gold, the samples were examined by SEM. The tissues around the samples from the experimental groups and negative control were collected as well. After fixing in 4% paraformaldehyde overnight and dehydration in gradient ethanol, the tissues were embedded in paraffin blocks. Histological longitudinal sections in a sagittal plane with a thickness of 5 μm were obtained and mounted on positively charged slides using the manual rotary microtome (RM2235, Leica, Germany). Afterwards, the slides were stained with hematoxylin-eosin (HE) and Gram staining and the images were captured by fluorescence microscopy (BX53, OLYMPUS, Japan).

2.3.4. *In vivo degradation behavior*

The corrosion products on the harvested sample were characterized by X-ray diffraction (XRD; D8 Advance, Bruker, Germany) and SEM. After removing he corrosion products with a chromic acid solution (200 g of CrO_3 and 10 g of $AgNO_3$ per liter of water), the surface topography of the samples was observed by SEM.

2.4. *In vitro cytocompatibility*

2.4.1. *Cell culture*

Mouse MC3T3-E1 pre-osteoblasts were cultured in α-MEM supplemented with 10% FBS and 1% penicillin and streptomycin at 37 °C in a 5% CO_2 humidified atmosphere. The medium was refreshed every 2 days and cell passages were performed while the cells proliferated to 80–90% confluence.

2.4.2. *Cell viability and cell adhesion assessment*

The cell viability was assessed by an extract assay. The extracts were prepared by soaking the PIII and untreated samples in the cell culture medium (α-MEM) with the sample surface area to extraction medium ratio of 1.25 ml · cm^{-2} according to ISO 10993–5 [21]. After 24 h, the supernatant fluid was collected and filtered for the cell viability assay. During the assay, the cells were cultured in a 96-well tissue culture plate at a density of 10^4 cells per well for 24 h to allow attachment. The medium was then replaced by extracts supplemented with 10% FBS and cultured for 24 h. Afterwards, the cells were washed with PBS and Cell Counting Kit-8 (CCK-8; Beyotime, China) was added to each well. After incubation for 4 h, the optical density at 450 nm was measured by a microplate reader (Multiskan GO, Thermo Fisher Scientific, USA). Cellular adhesion was evaluated using actin and nucleus staining. The MC3T3-E1 cells were seeded on the PIII and untreated samples with a density of 5×10^4 cells per well in 24-well plates and incubated for 5 and 24 h, respectively. Afterwards, the cells were fixed and permeabilized successively with the 4% paraformaldehyde (PFA) diluent and 0.1% (v/v) Triton X-100 (Amresco, USA). The cytoskeleton F-actin protein and nuclei of the cells were stained with rhodamine labelled phalloidin and DAPI and observed under a fluorescence microscope (BX53, Olympus, Japan).

2.5. *Statistical analysis*

All of the *in vitro* experiments were performed in triplicate and the data were reported as mean ± standard deviation (SD). The statistical analysis was conducted by SPSS (SPSS 17.0 Inc., Chicago, USA). The student's t-test and one-way analysis of variance (ANOVA) were used to evaluate the difference between groups and a p value < 0.05 was considered to be statistically significant.

3. Results

3.1. *Sample characterization*

The AFM images of the ZK60 samples before and after PIII in Fig. 1a reveal obvious changes in the surface topography after the plasma treatment. There are some scratches from mechanical grinding on the untreated surface but the surface becomes smoother after Zr PIII with only slightly wavy protrusions. After O PIII, the sample surface is smoother and more compact than the Zr PIII and untreated ones. The average surface roughness values of the untreated, Zr PIII, and Zr & O PIII samples are 12.50, 7.84 and 2.93 nm, respectively (Fig. 1b). The decreased surface roughness after PIII may be attributed to high-energy ion bombardment. A smoother and more compact surface usually offers better corrosion resistance and thus the diminished surface roughness resulting from PIII is expected to mitigate degradation. Fig. 1c shows the average water contact angles of the Zr & O PIII, Zr PIII and untreated samples are 106.6°, 104.4°, and 42.4°, respectively. A larger contact angle is related to lower surface free energy thus indicating that the PIII surface is more hydrophobic [22]. Fig. 1d shows the surface hardness and elastic modulus of the Zr & O PIII, Zr PIII and untreated samples. Zr & O PIII sample shows the largest surface hardness and elastic modulus, followed by Zr PIII and the untreated samples which has the least surface hardness and elastic modulus. Hence, Zr & O PIII improves the surface mechanical properties of ZK60.

In order to investigate the crystal structure and composition of the Zr & O PIII film, cross-sectional TEM, EDS, HRTEM and SAED are carried out. As shown in the TEM image and EDS maps (Fig. 2a and b), a layer composed of Mg, O and Zr with a thickness of 30 nm is formed on the ZK60 magnesium alloy after PIII. The HRTEM image (Fig. 2c) taken from area **I** in Fig. 2a exhibits the typical crystallographic orientation of MgO (400), MgO (200) and ZrO_2 (210), confirming the oxide composition of the PIII film. Fig. 2c clearly shows that MgO (400) is adjacent to ZrO_2 (210), which can result in lattice distortion in the area due to their different lattice constant. In addition, some areas marked with red circles become dim and disordered, which might be attributed to the formation of local oxygen vacancies under high-energy ion bombardment. The well-defined electron diffraction spots correlate with the crystalline

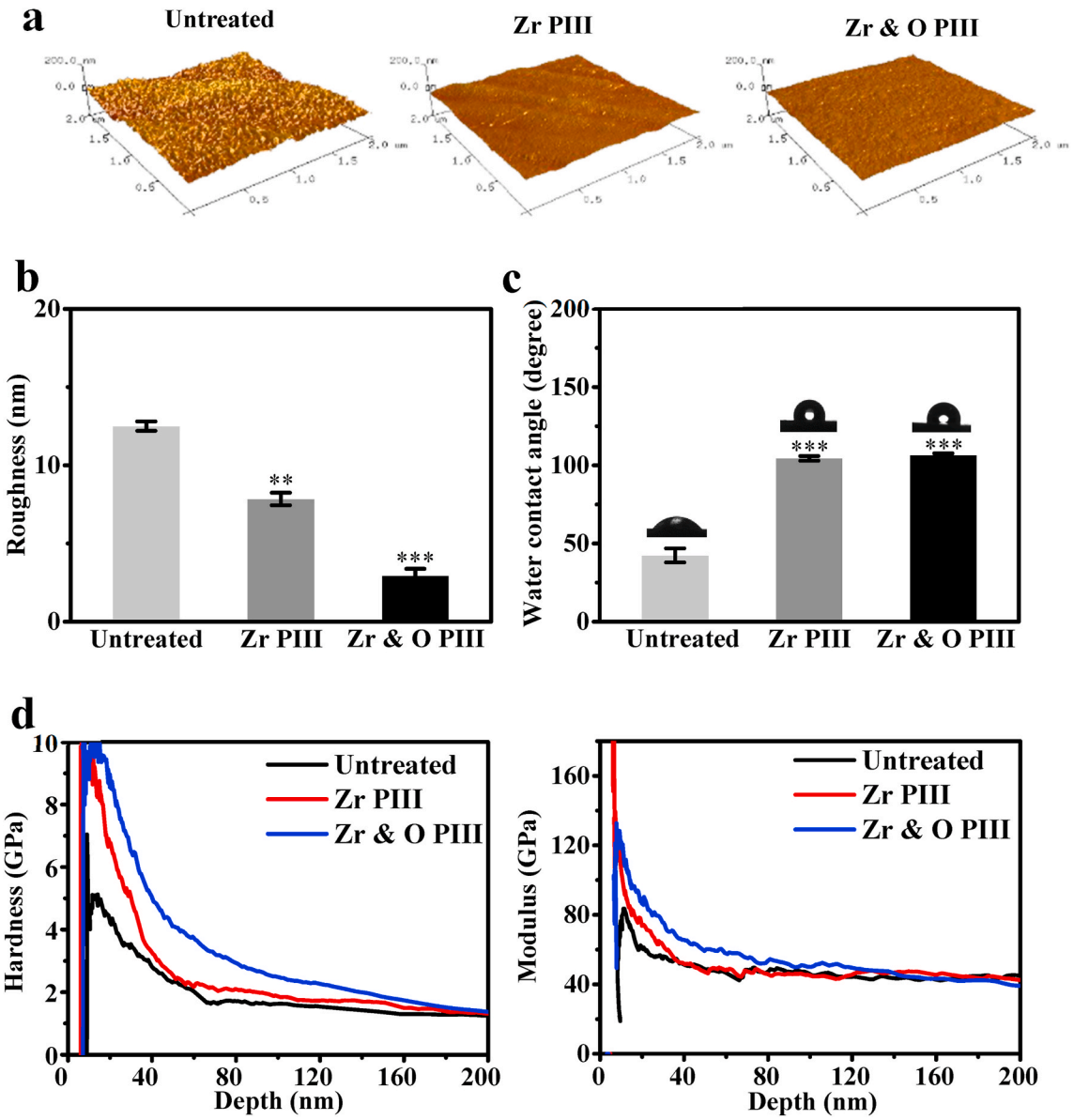

Fig. 1. Characterization of the Zr & O PIII, Zr PIII and untreated samples: (a) AFM images; (b) Surface roughness; (c) Water contact angles; (d) Surface hardness and elastic modulus. The results are presented as mean ± SD with $^{**}p < 0.01$, $^{***}p < 0.001$.

nature of the face-centered cubic phase of MgO and orthorhombic phase of ZrO_2. The SAED patterns corresponding to area **I** show typical diffuse diffraction rings indicating the nanocrystal structure of the oxide film (Fig. 2d). Fig. 2e shows the SAED patterns obtained from area **II** in Fig. 2a. It reveals typical hexagonal Mg with indexed as the zone axis [001] and planes of (110) and ($\bar{2}$10) consistent with the standard card (JCPDS 35–0821) of Mg.

The high-resolution XPS Mg 1s, Zr 3d, and O 1s spectra acquired from the Zr & O PIII sample at different sputtering time are displayed in Fig. 3a. The binding energy (BE) of the Mg 1s in the top surface zone is about 1304.3 eV arising from Mg^{2+} of MgO [23]. After sputtering for 6 min, the Mg 1s peak shifts to higher BE with sputtering time. While sputtering for 8 min, the binding energy for Mg 1s peak located at 1305.2 eV (Fig. 3b). In contrast, the Zr $3d_{5/2}$ and Zr $3d_{3/2}$ spectra exhibit the same peak shift as Mg 1s. Before the sputtering time is increased to 16 min, the Zr^{4+} peak gradually shifts towards higher BE with sputtering time, indicating that the chemical state of Zr^{4+} species in the deeper layer is different from that in the superficial layer. The shift to higher BE for the Mg^{2+} and Zr^{4+} peaks may be attributed to the formation of oxygen vacancies. When the sputtering time is 16 min, the Mg 1s and Zr 3d peaks at BE of 178.7 and 1302.5 eV, respectively, shift oppositely to lower binding energies and the valence states of zirconium and magnesium gradually change from the oxidized states (Zr^{4+} and Mg^{2+}) to metallic ones (Zr^0, and Mg^0), suggesting formation of a graded modified layer. As shown in the high resolution XPS O 1s spectra as well as depth profiles, an oxygen rich layer is formed on the surface. The main peak of O 1s is variable with sputtering depth, indicating the multi-component oxygen species are present in the surface. The O 1s spectra after sputtering for 8 min can be divided into two different oxygen-containing functional groups (Fig. 3b). The lower BE of the O 1s at 530.5 eV is denoted as O^{2-} species in metal oxide and the higher BE at 531.3 eV may be related to oxygen vacancies (O_v) in mixed oxide. Fig. 3c show XPS depth profiles of Mg, O and Zr elements. The percentage of Mg content increases gradually as it approached to the substrate, while the percentage of O and Zr contents decrease gradually. When the sputtering time is increased up to 16 min at the position of the substrate, O and Zr contents decrease to almost zero. Fig. 3d shows the UV–vis DRS spectra of the PIII and untreated samples. The spectra of Zr PIII and untreated

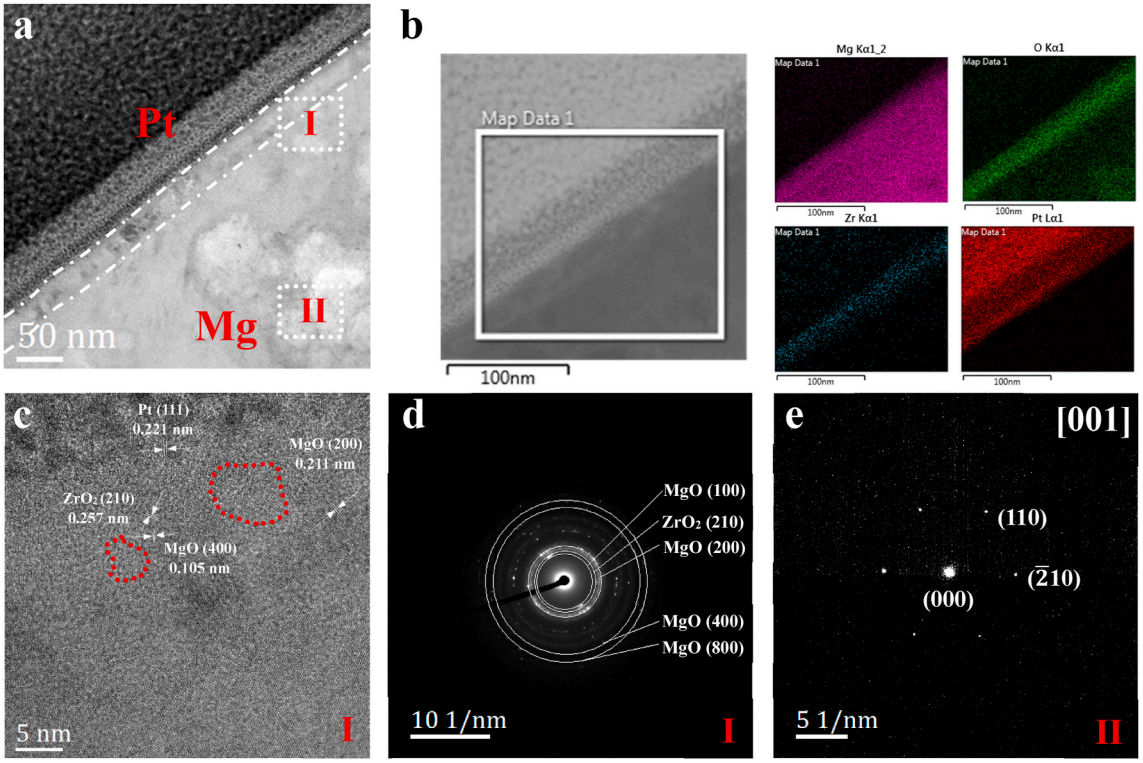

Fig. 2. Structural and morphological characterization of the Zr & O PIII sample: (a) Cross-sectional TEM image; (b) EDS mapping analysis; (c) HRTEM image from area **I**; (d) SAED pattern from area **I**; (e) SAED pattern from area **II**.

samples exhibit an intense absorption band at 290 nm, while the band shifts to around 405 nm for the Zr & O PIII sample. It is obvious that the absorption band edge of the Zr & O PIII sample exhibits a red-shift to the visible region (400–600 nm). The possible reason is the high concentration of oxygen vacancies formed in the Zr & O PIII films. In addition, the room-temperature EPR spectra of the PIII samples are shown in Fig. 3e. An absorption band indicative of oxygen vacancies at g = 2.004 presents in the Zr & O PIII and Zr PIII samples, but not in the untreated one. The typical signal for characteristic of oxygen vacancies is significantly enhanced for the Zr & O PIII sample compared to the Zr PIII one, which suggests that high concentration of oxygen vacancies were formed in the Zr & O PIII films. The EPR results further confirm the analysis of XPS spectra and UV–vis spectra.

3.2. In vitro degradation

Fig. 4a depicts the representative polarization curves of the Zr & O PIII, Zr PIII and untreated samples in SBF and TSB. The corrosion potential and corrosion current density can be derived directly from the cathodic/anodic polarization curves by Tafel extrapolation. According to the deduction from the cathodic curves acquired in SBF, the corrosion current densities of the Zr & O PIII, Zr PIII, and untreated samples are 1.02×10^{-4}, 1.71×10^{-4} and 7.40×10^{-4} A · cm^{-2}, respectively, presenting an increasing trend. Similarly, the corrosion current densities acquired from the polarization curves of the Zr & O PIII, Zr PIII, and untreated samples in TSB are 1.93×10^{-5}, 3.02×10^{-5} and 1.42×10^{-4} A · cm^{-2}, respectively. The corrosion rate can be received according to the following equation.

$$P_i = \frac{M \times i_{corr}}{n \times F \times \rho} \times 87600 \quad (1)$$

Where P_i represents average corrosion rate (mm · y^{-1}), i_{corr} is the corrosion current density evaluated by Tafel extrapolation of the cathodic polarization curve, M is the molar mass (M_{Mg} = 24.31 g · mol^{-1}), n is the number of electrons involved in the corrosion reaction, F is the Faraday's constant (26.8 A · h), ρ is the standard density of the magnesium alloy (ρ_{ZK60} = 1.82 g · cm^{-3}) [24]. The result shows that the corrosion rate of Zr & O PIII, Zr PIII and untreated sample in the SBF is 2.2, 3.7 and 16.2 mm · y^{-1}, respectively, and that in the TSB is 0.4, 0.7 and 3.1 mm · y^{-1}, respectively. The cathodic polarization curve is considered to represent the cathodic hydrogen evolution, whereas the anodic one represents dissolution of magnesium [25,26]. Our results suggest that the hydrogen evolution rate and degradation rate of the PIII samples are less than those of the untreated, especially the Zr & O PIII sample, which shows the smallest degradation rate.

The Nyquist plots of the PIII samples after immersion in SBF and TSB are displayed in Fig. 4a and the three loops suggest three time constants. The higher frequency capacitive loop is associated with the charge transfer resistance, the capacitive loop in the medium frequency region is attributed to mass transport in the solid phase, and the inductive loop in the lower frequency is attributed to the adsorption process. Regardless of the media, the EIS spectra of Zr & O PIII sample shows larger capacitive loop and inductive loop diameter than Zr PIII and untreated samples. It is well known that a larger diameter arc suggests better corrosion resistance and therefore, it can be concluded from the EIS results that Zr & O PIII produces more corrosion resistance. The equivalent circuit in the Nyquist plots is proposed to fit the Nyquist plots and Table 1 shows the fitted EIS results. The experimental and fitted data show good agreement with χ^2 of 2.97×10^{-4}. R_s represents the electrolyte resistance between the reference electrode and working electrode. CPE_1 and R_1 represent the capacitance and the resistance of the surface film. CPE_2 represents the capacitance of the double layer and R_2 is the charge transfer resistance, and L and R_L represent the inductance and inductive resistance [27,28]. The CPE value is defined by two values, Q and n, where Q is the admittance constant of the CPE and n is the index of the dispersion effects of CPE representing deviations from the ideal capacitance due to the inhomogeneity and roughness of the electrode on the micro scale. Larger R_1 and R_2 suggest the formation of a

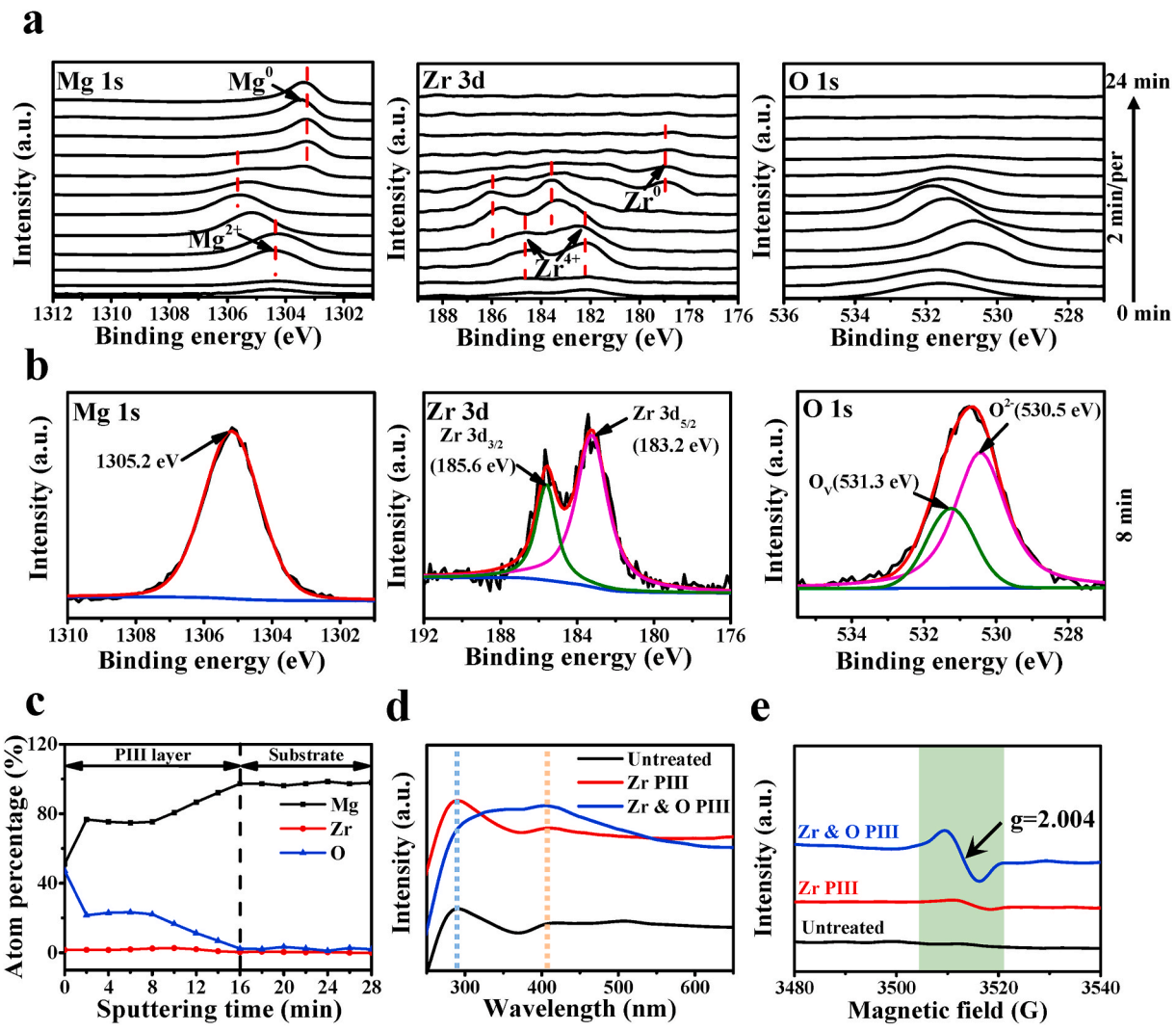

Fig. 3. Identification of oxygen vacancies in the Zr & O PIII sample: (a) High-resolution XPS spectra at various sputtering time; (b) High-resolution XPS spectra (sputtering for 8 min); (c) XPS depth profiles; (d) UV–vis DRS spectra; (e) Solid EPR spectra.

more compact surface film on the surface and higher resistance to magnesium dissolution [29,30]. In this study, introduction of Zr and formation of the ZrO_2 containing films provide effective protection on the magnesium substrate thus enhancing the surface corrosion resistance. In addition, the diminished surface roughness and enhanced compactness after PIII play important roles in the corrosion resistance [30–32]. Overall, the data confirm that the best protection is achieved after dual Zr & O PIII.

Fig. 4b compares the leached Mg and Zr ion concentrations between PIII and untreated samples in PBS at 6 and 12 h. The amount of magnesium released from PIII samples is less than the untreated group, suggesting that degradation of magnesium alloy is inhibited after PIII. However, the Zr ion concentration from the PIII group is more than that from the untreated group because of introduction of Zr by PIII. In addition, the Mg and Zr ion concentration increase from 6 to 12 h is less than from 0 to 6 h, indicating that ion release slows gradually with immersion time.

3.3. *In vitro antibacterial properties*

The ability of the PIII ZK60 magnesium alloys to prevent bacterial adhesion is evaluated by fluorescence microscopy and SEM. As shown in Fig. 5a, after culturing for 6 h, there are a large amount of viable bacteria on the untreated group but there are less on the Zr PIII group. In comparison, the amounts of adherent bacteria are much less on Zr & O PIII group and most of them are dead. Similarly, the SEM images reveal less adherent bacteria on Zr & O PIII group than Zr PIII and untreated groups. Our results suggest that Zr & O PIII enhances the bacterial resistance of ZK60. In addition, the SEM images reveal a large amount of corrosion products on the untreated sample, whereas Zr & O PIII sample only shows small local cracks suggesting effective protection by the graded oxide films. The antibacterial rates of the PIII and untreated samples against *S. aureus* determined by the spread plate method are exhibited in Fig. 5b. The Zr & O PIII group shows significantly higher antibacterial rates than the Zr PIII and untreated group. Fig. 5c shows the intracellular ROS fluorescent images of the PIII and untreated groups. The fluorescent intensity of intracellular ROS reveals obvious increase for the PIII and untreated groups from 1 h to 6 h. According to quantitative analysis of the intracellular ROS in Fig. 5d, the untreated group shows higher ROS signals than the Zr PIII and Zr & O PIII groups after 1 h. However, a distinguishably higher level of ROS expression appears after 3 and 6 h for the Zr & O PIII group compared to Zr PIII and untreated groups. Thus, intracellular ROS induced by Zr & O PIII should be responsible for the antibacterial effects. Fig. 5e shows the qRT-PCR results of *icaADBC* and *icaR* genes expression of the *S. aureus* co-cultured with Zr & O PIII, Zr PIII, and untreated samples for 24 h. The results show that the expressions of *icaADBC* genes are down-regulated and *icaR* gene is up-regulated for *S. aureus* co-cultured with the

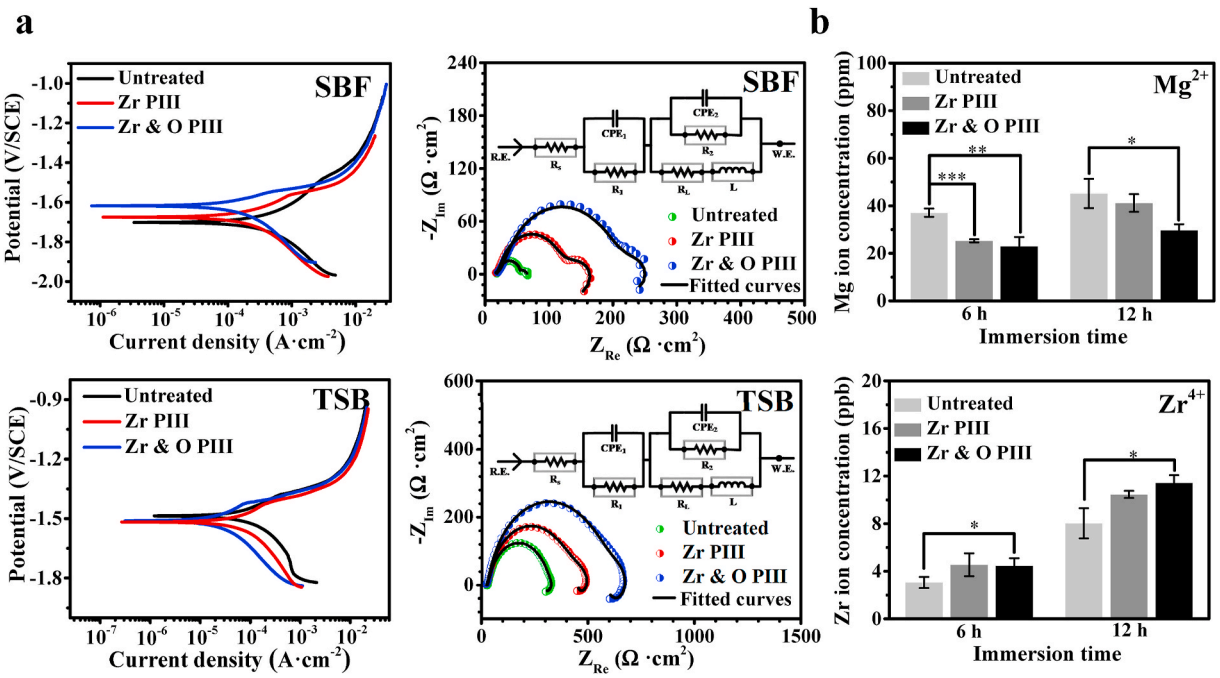

Fig. 4. *In vitro* degradation examination of the Zr & O PIII, Zr PIII, and untreated samples: (a) Polarization curves, EIS spectra, and corresponding equivalent circuit (inset) of the samples immersed in SBF and TSB; (b) Mg^{2+} and Zr^{4+} concentrations measured after immersion for 6 and 12 h in PBS. The results are presented as mean ± SD with $^*p < 0.05$, $^{**}p < 0.01$ and $^{***}p < 0.001$.

Table 1
Fitted EIS results of the Zr & O PIII, Zr PIII, and untreated samples in SBF and TSB.

	SBF			TSB		
	Untreated	Zr PIII	Zr & O PIII	Untreated	Zr PIII	Zr & O PIII
R_S (Ω · cm^2)	17.63	14.32	15.76	26.58	20.18	20.08
CPE_1 (Ω^{-2} · cm^{-2} · S^{-n})	8.08 × 10^{-4}	1.27 × 10^{-5}	2.90 × 10^{-5}	1.65 × 10^{-5}	1.33 × 10^{-3}	1.61 × 10^{-3}
n_1	0.5321	1	0.3244	0.9943	0.4676	0.4454
R_1 (Ω · cm^2)	43.36	72.64	144.2	183.2	300.9	432.3
CPE_2 (Ω^{-2} · cm^{-2} · S^{-n})	1.82 × 10^{-5}	3.60 × 10^{-3}	1.54 × 10^{-5}	2.32 × 10^{-4}	1.86 × 10^{-5}	1.50 × 10^{-5}
n_2	1	0.3346	0.9341	0.6591	0.9537	0.9359
R_2 (Ω · cm^2)	15.39	111.5	141.7	121	310	475.5
L (H · cm^2)	0.08376	239.8	664.8	539.9	534.9	918.8
R_L (Ω · cm^2)	8.404	62.23	211.3	256.8	409.5	494

untreated ZK60 compared to the TSB control, confirming that magnesium alloys have antimicrobial properties *in vitro*. Furthermore, the Zr PIII and Zr & O PIII groups inhibit biofilm formation by down-regulating the expression level of *icaADBC* genes but up-regulating the expression levels of *icaR* gene compared with the untreated and TSB control, revealing superior antibacterial performance of the magnesium alloys after PIII.

3.4. *In vivo* antibacterial properties

Fig. 6a presents schematic illustration of hypodermic implantation of SD rats. After *in vivo* culturing for 3 and 7 days, the spread plate method is used to count the bacteria adhered to the implant surfaces. Fig. 6b shows that the number of bacterial colonies on the Zr & O PIII group is significantly less than that on the untreated group after 3 and 7 days, suggesting enhanced *in vivo* antibacterial rate due to Zr & O PIII. By increasing the culture time from 3 to 7 days, the bacterial colony numbers on the Zr & O PIII and untreated groups increase because long-term *in vivo* culture suppresses degradation of the magnesium alloy and diminishes the *pH* so that the antibacterial ability of ZK60 decreases. On the other hand, long-term *in vivo* culture on the corroded and destroyed Zr & O implanted layer shows that the antibacterial protection weakens. Fig. 7a shows the SEM images of the Zr & O PIII and untreated samples 3 and 7 days after operation. There are sporadic bacteria on the Zr & O PIII samples, but in contrast bacteria adhered onto the untreated sample are more and aggregate to form biofilms after 7 days. The results indicate that the Zr & O PIII implanted layer inhibits bacteria adhesion and biofilm formation *in vivo*.

3.5. *In vivo* degradation property

The surface morphology as well as phase composition of the Zr & O PIII and untreated sample at 3 and 7 days post-surgery are shown in Fig. 7. According to the XRD patterns in Fig. 7b, the corrosion products formed on the Zr & O PIII and untreated samples are composed of Mg $(OH)_2$ and $(Mg, Ca)_3(PO_4)_2$. The cross-sectional view of the Zr & O PIII and untreated samples at 3 and 7 days post-operation is shown in Fig. 7c. A porous and inhomogeneous corrosion product layer is formed on the Zr & O PIII and untreated samples. The thicknesses of the corrosion product layer on the Zr & O PIII sample are 13 and 25 μm at 3 and 7 days post-operation, whereas those on the untreated sample are 20 and 69 μm, respectively. The average general corrosion rates were further calculated according to the thickness of corrosion product layer divided by exposure time [33] and the corresponding results are shown in Fig. S1. At 3 days post-operation, the average corrosion rate of the Zr & O PIII and untreated samples is 0.1 and 0.2 mm · y^{-1}, respectively. In comparison, at 7 days post-operation, the average corrosion rate of the Zr & O PIII and untreated samples is 0.5 and 1.3 mm · y^{-1}, respectively. It is obvious that the degradation of both samples is aggravated with the

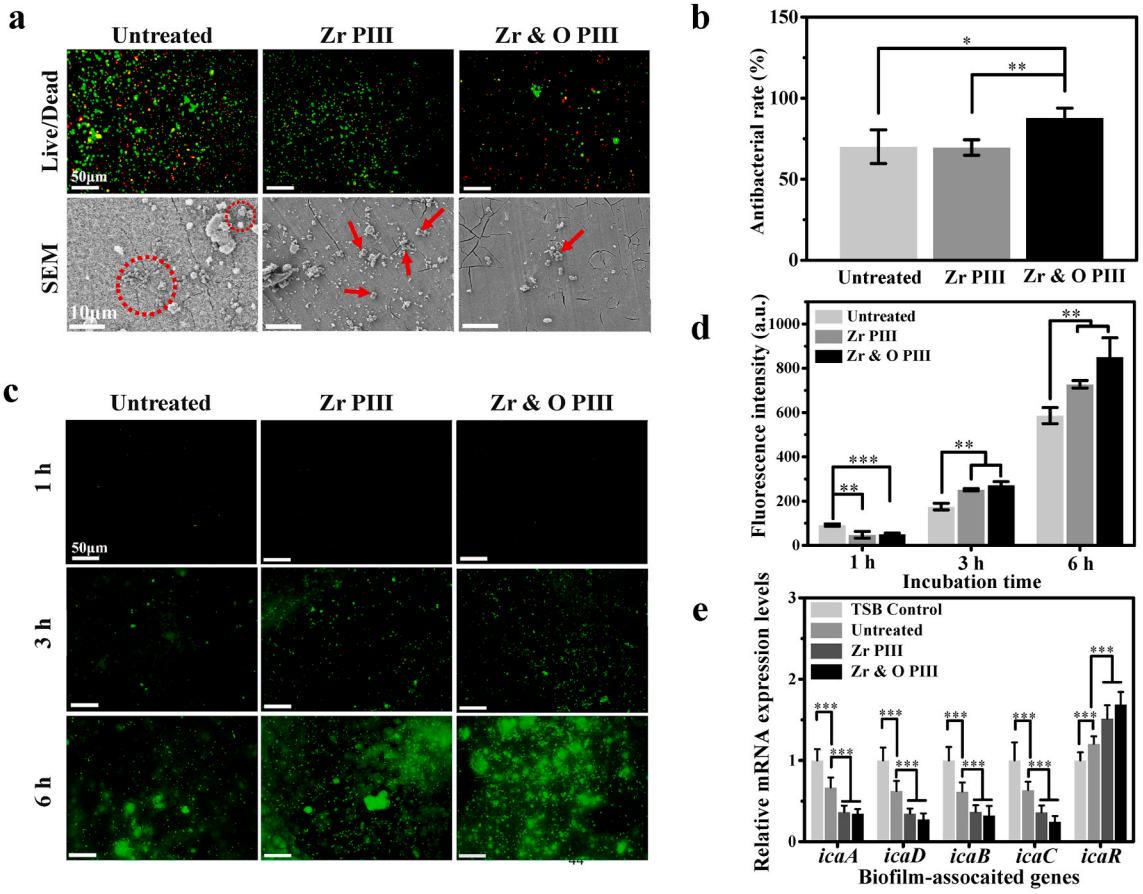

Fig. 5. *In vitro* antibacterial performance of the Zr & O PIII, Zr PIII, and untreated samples: (a) Live/Dead fluorescence images and SEM images (red circles or arrows represent bacteria); (b) Antibacterial rates; (c) Fluorescence images of intracellular ROS; (d) Quantitative analysis of intracellular ROS; (e) qRT-PCR analysis of *icaADBC* and *icaR* genes. The results are presented as mean ± SD with $*p < 0.05$, $**p < 0.01$, and $***p < 0.001$.

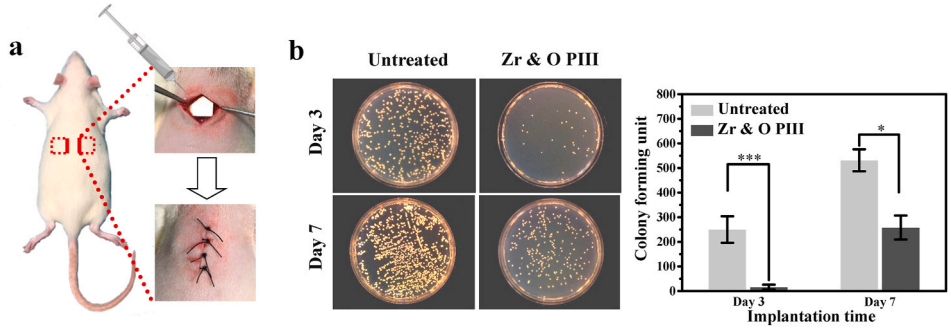

Fig. 6. *In vivo* antibacterial performance of the Zr & O PIII implants at 3 and 7 days post-operation: (a) Schematic illustration of the surgical procedure using the rat model; (b) Representative images and quantitative analysis of viable bacteria cultured on the sample surfaces by the spread plate method. The untreated samples are used as the control group. The results are presented as mean ± SD with $*p < 0.05$, and $***p < 0.001$.

increase of implantation time. But compared to the untreated sample, the Zr & O PIII sample reveals significantly slower degradation rate. It suggests that Zr & O PIII provided effective protection to ZK60 magnesium during the early stage of implantation. The surface morphology of the samples after removing the corrosion product are depicted in Fig. 7d. A number of small and shallow corrosion pits are distributed on the untreated sample at 3 days post-operation. After 7 days, the corrosion pits become larger and deeper. At the same time point, the Zr & O PIII samples exhibit slight corrosion with shallower and smaller corrosion pits compared to the untreated samples. Hence, degradation of the ZK60 magnesium alloy is retarded by Zr & O PIII.

3.6. Histological analysis

HE staining of the tissues surrounding the implants at 3 and 7 days post-operation is carried out to investigate inflammation as shown in Fig. 8. Local inflammation tissues with purple color are shown around the untreated implants. Larger area of inflammation tissue can be observed at 7 days post-operation than at 3 days, implying that inflammation reaction become more serious with time. In contrast, inflammation reaction in the Zr & O PIII group is milder than the untreated group at each time point. Even at 7 days after implantation, only a small amount of inflammatory tissues can be observed. Gram staining discloses that several bacteria communities (dark purple spots where the

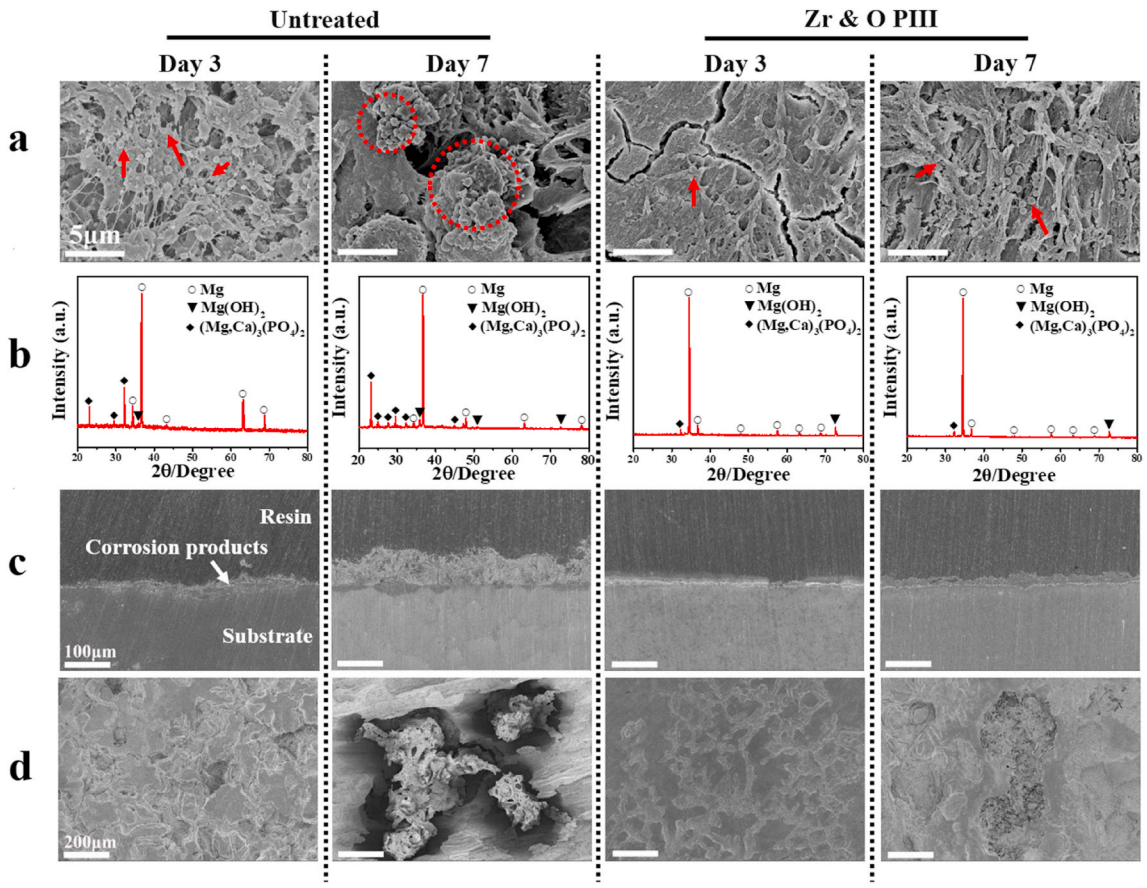

Fig. 7. *In vivo* degradation behavior of the Zr & O PIII and untreated implants at 3 and 7 days post-operation: (a) Surface morphology (Red circle and arrows representing bacteria); (b) X-ray diffraction patterns; (c) Cross-sectional views; (d) Surface morphology of the implants after removing the corrosion products.

arrows represent) in the tissues surround the untreated implant both at 3 and 7 days post-operation. However, no bacteria are found from the Zr & O PIII group. The histological findings suggest that Zr & O PIII diminishes the inflammation reaction of magnesium alloys. However, it is difficult to tell whether the inflammation effect is attributed to the foreign-body reaction or bacterial infection. Thus, a nonbacterial animal model is used to evaluate the foreign body reaction of the tissues surrounding the implants and the corresponding HE staining histological images are shown in Fig. S2. The results show that no inflammatory reactions are found from the tissues surrounding the Zr & O PIII and untreated implants suggesting the absence of foreign-body reactions for both groups. All in all, bacterial infection causes inflammation and Zr & O PIII promotes the antibacterial ability of the magnesium alloys.

3.7. Cytocompatibility

The cell viability of the Zr & O PIII, Zr PIII and untreated samples is presented in Fig. S3a. The cells cultured in the extracts of the Zr PIII and untreated samples show low cell viability below 70%. In comparison, the cell viability of Zr & O PIII is about 95% implying improved cytocompatibility. Fig. S3b presents the fluorescent images of MC3T3-E1 cells adhered to the Zr & O PIII, Zr PIII and untreated samples after culturing for 5 and 24 h. As shown in Fig. S3b, only a few cells adhere to the Zr PIII and untreated samples after 5 h and most of the cells fail to spread well. After 24 h, the cells transform from the polygonal shape to round shape, revealing the characteristics of dead cells. In contrast, the attached cells on the Zr & O PIII sample exhibit more obvious filopodia and flattened membranes even after 24 h suggesting better cytocompatibility after Zr & O PIII.

4. Discussion

Mg alloys possess antibacterial functions due to degradation in the bacterial solution resulting in rapid increase in the local *pH* [10]. In our study, even though degradation of ZK60 is retarded by PIII, Zr & O PIII ZK60 still shows remarkable antibacterial characteristics. It is obvious that the antibacterial properties do not originate from the alkaline environment but rather combined effects of the altered surface chemical composition, roughness, and surface hydrophobicity after PIII.

Because bacteria in a biofilm are more resistant to treatment with antibiotics than their planktonic counterparts, routine antibiotic treatments are usually incapable of reducing implant-associated infection and implant removal is usually the only effective way to eradicate the problem [34–36]. The antibacterial mechanism of Zr & O PIII is illustrated in Fig. 9. Previous reports have shown that zirconium and zirconium oxide can inhibit bacteria colonization on the surface. Al-Radha et al. [37] reported that pure zirconia and titanium blasted with zirconia showed superior performance in reducing the adhesion of bacteria to the smooth surface and Rimondini et al. [38] found that two types of zirconia surfaces showed significantly less bacteria adhesion than titanium in their *in vivo* experiments as dental implants. Avila et al. [39] demonstrated that the ZrO_2 implant abutment surfaces showed decreased anaerobic biofilm than Ti and bovine enamel, and Li et al. illustrated that Zr PIII treated CFR-PEEK with ZrO_2 nanostructures exhibited obvious antibacterial activity against *S. aureus* [40]. In our study, introduction of zirconium and formation of zirconium oxide by PIII are the main reasons for the enhancement of the antibacterial property. It is attributed to not only the intrinsic antibacterial characteristics of zirconium and zirconium oxide, but also higher concentration of oxygen vacancies formed by PIII.

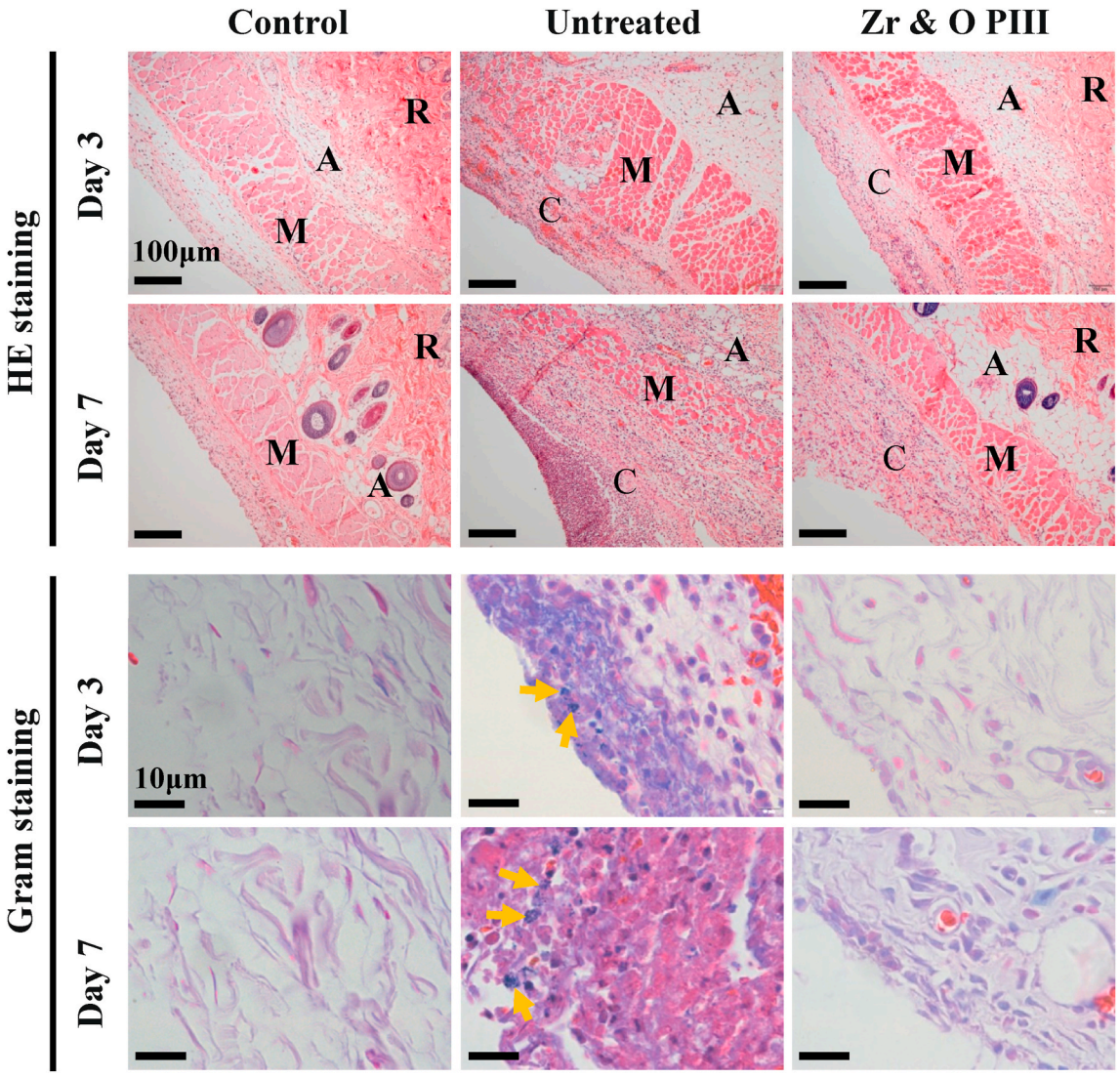

Fig. 8. Histological analysis of the infectious tissues surrounding the Zr & O PIII and untreated implants at 3 and 7 days post-operation by HE staining and Gram staining. Normal tissues are used as the control. R, A, M and C represent the reticular region, adipose tissue, muscle layer and connective tissue layer, respectively. The yellow arrows represent *S. aureus*.

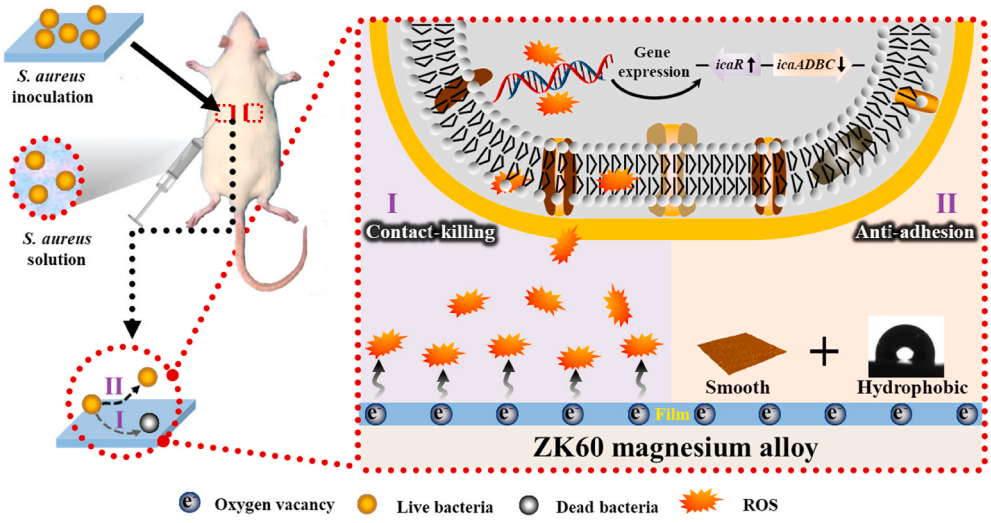

Fig. 9. Schematic process illustrating the possible antibacterial mechanism of the Zr & O PIII ZK60 magnesium alloy.

According to HRTEM image, local areas of Zr & O PIII layer become dim and disordered, which might be pertinent to the formation of surface oxygen vacancies [41,42]. In addition, XPS spectra and UV–vis spectra of Zr & O PIII sample also suggested the formation of oxygen vacancies based on the existence of characteristic peak of oxygen vacancies at the BE of 531.3 eV and the redshift of the absorption band edge, respectively [43,44]. On one hand, the oxygen vacancies changed the coordination of O atoms, which resulted in the decrease of electron density around O atoms, and thus revealing a high electron-attracting effect with high BE in the XPS spectra [45,46]. On the other hand, while lots of oxygen vacancies exist, the oxygen vacancy states become nonlocalized and overlap with the valence band edge, thus leading to a rise in the valence band and a narrowing of the band gap increasingly [44,47]. And band-gap narrowing usually causes the redshift of the absorption band edge in UV–vis spectra [48,49]. In addition, EPR is an effective way to determine in situ oxygen vacancy [50]. Our results showed that the typical signal of oxygen vacancies was significantly enhanced for Zr & O PIII sample compared to Zr PIII and untreated samples, suggesting that high concentration of oxygen vacancies were formed in the PIII films. PIII is a high-energy ion bombardment process. During the Zr & O PIII process, Zr and O elements are introduced into the surface film. Zr atoms might occupy the location of Mg atoms in the lattice of MgO, which lead to the formation of oxygen vacancies to compensate the charge balance [43]. On the other hand, continuous high-energy ion bombardment might directly remove oxygen from the lattice of oxide and generate oxygen vacancies [51].

The oxygen vacancies have been reported to induce ROS generation to enhance the antibacterial properties [50,52]. In the present study, high concentration of oxygen vacancies in the Zr & O PIII film promote the generation of intracellular ROS of *S. aureus* presenting significantly up-regulated ROS expression, which further inhibits the biofilm formation (Fig. 5). This is because that ROS accumulation may negatively affect the expression of *S. aureus* biofilm-associated genes. It is assumed that biofilm formation depends on the synthesis of polysaccharide intercellular adhesin (PIA) [53,54]. PIA, a kind of polysaccharides, is one of the major constituents of *S. aureus* biofilms. PIA-associated *S. aureus* biofilm formation is mediated by the intercellular adhesin (*ica*) locus, which consists of five genes: *icaR*, *icaA*, *icaD*, *icaB* and *icaC* [55]. The *icaR* gene is a negative regulator of *icaADBC* genes [55]. It is assumed that the inhibition of *icaADBC* genes expression and increase of *icaR* gene expression downregulate the production of PIA, thereby reducing biofilm formation [56]. In this study, down-regulated expression of *icaADBC* as well as up-regulated expression of *icaR* genes were presented for Zr & O PIII magnesium alloy (Fig. 5e), confirming ROS mediated biofilm-associated genes expression inhibits biofilm formation. Thus, the Zr & O PIII ZK60 magnesium alloy has better *in vitro* and *in vivo* antibacterial performance.

In addition, the enhanced surface hydrophobicity and smaller surface roughness after Zr & O PIII also inhibit bacterial adhesion on the sample. It has been shown that a surface with higher surface energy is more prone to bacterial adherence [57,58]. Moreover, bacteria cells prefer to anchor on a rough surface since they can be pressed into the grooves to be better sheltered from displacing shear forces to transit from reversible to irreversible adhesion [59]. Regarding the effects of surface roughness on bacterial attachment, it is believed that the smoother surface formed by Zr & O PIII negatively impacts bacterial colonization. All in all, our study reveals that bacteria have less affinity and higher mortality rates on the ZrO_2-containing ZK60 with high concentration of oxygen vacancies, low surface roughness, and high surface hydrophobicity.

5. Conclusion

Dual Zr and O plasma immersion ion implantation is performed to modify ZK60 magnesium alloy. A hydrophobic, smooth, and ZrO_2-containing surface graded film is formed to enhance *in vitro* and *in vivo* bacterial resistance. The enhanced antibacterial properties are attributed to the synergetic effects of the formed high concentration of oxygen vacancies in the ZrO_2-containing surface films as well as enhanced surface hydrophobicity and decreased surface roughness. Our study reveals an effective technique for magnesium alloy to achieve superior antibacterial properties.

CRediT authorship contribution statement

Tao Liang: Conceptualization, Methodology, Validation, Formal analysis, Investigation, Data curation, Writing – original draft, Writing – review & editing. **Lilan Zeng:** Methodology, Validation, Investigation, Writing – original draft. **Yunzhu Shi:** Data curation, Writing – review & editing. **Haobo Pan:** Supervision, Project administration. **Paul K. Chu:** Resources, Supervision. **Kelvin W.K. Yeung:** Data curation. **Ying Zhao:** Conceptualization, Data curation, Supervision, Writing – original draft, Writing – review & editing, Project administration, Funding acquisition.

Declaration of competing interest

The authors declare that there is no known conflict of interest that could influence the findings reported in this paper, neither at personal nor at organizational level.

Acknowledgements

The study was financially supported by the National Natural Science Foundation of China (51501218), Shenzhen Science and Technology Research Funding (JCYJ20160608153641020), as well as Hong Kong Research Grants Council (RGC) General Research Funds (GRF) No. CityU 11301215.

Appendix A. Supplementary data

Supplementary data related to this article can be found at https://doi.org/10.1016/j.bioactmat.2021.02.025.

References

[1] Y. Wang, W. Teng, Z. Zhang, X. Zhou, Y. Ye, P. Lin, A. Liu, Y. Wu, B. Li, C. Zhang, X. Yang, W. Li, X. Yu, Z. Gou, Z. Ye, A trilogy antimicrobial strategy for multiple infections of orthopedic implants throughout their life cycle, Bioact. Mater. 6 (2021) 1853–1866, https://doi.org/10.1016/j.bioactmat.2020.11.030.

[2] C.R. Arciola, D. Campoccia, L. Montanaro, Implant infections: adhesion, biofilm formation and immune evasion, Nat. Rev. Microbiol. 16 (2018) 397–409, https://doi.org/10.1038/s41579-018-0019-y.

[3] M. Martinez-Perez, A. Conde, M.A. Arenas, I. Mahillo-Fernandez, J.J. de-Damborenea, R. Perez-Tanoira, C. Perez-Jorge, J. Esteban, The "Race for the Surface" experimentally studied: *In vitro* assessment of *Staphylococcus spp.* adhesion and preosteoblastic cells integration to doped Ti-6Al-4V alloys, Colloids Surf. B 173 (2019) 876–883, https://doi.org/10.1016/j.colsurfb.2018.10.076.

[4] S. Yuran, A. Dolid, M. Reches, Resisting bacteria and attracting cells: spontaneous formation of a bifunctional peptide-based coating by on-surface assembly approach, ACS Biomater. Sci. Eng. 4 (2018) 4051–4061, https://doi.org/10.1021/acsbiomaterials.8b00885.

[5] M. Ghasemlou, F. Daver, E.P. Ivanova, J.W. Rhim, B. Adhikari, Switchable dual-function and bioresponsive materials to control bacterial infections, ACS Appl. Mater. Inter. 11 (2019) 22897–22914, https://doi.org/10.1021/acsami.9b05901.

[6] Y. Zhao, L.L. Zeng, T. Liang, Development in biocompatibility of biodegradable magnesium-based metals, Acta Metall. Sin. 53 (2017) 1181–1196, https://doi.org/10.11900/0412.1961.2017.00259.

[7] N. Zhang, W. Wang, X. Zhang, K.C. Nune, Y. Zhao, N. Liu, R.D.K. Misra, K. Yang, L. Tan, J. Yan, The effect of different coatings on bone response and degradation behavior of porous magnesium-strontium devices in segmental defect regeneration, Bioact. Mater. 6 (2021) 1765–1776, https://doi.org/10.1016/j.bioactmat.2020.11.026.

[8] J. Gao, Y. Su, Y.X. Qin, Calcium phosphate coatings enhance biocompatibility and degradation resistance of magnesium alloy: correlating *in vitro* and *in vivo* studies, Bioact. Mater. 6 (2021) 1223–1229, https://doi.org/10.1016/j.bioactmat.2020.10.024.

[9] D. Zhao, F. Witte, F. Lu, J. Wang, J. Li, L. Qin, Current status on clinical applications of magnesium-based orthopaedic implants: a review from clinical translational perspective, Biomaterials 112 (2017) 287–302, https://doi.org/10.1016/j.biomaterials.2016.10.017.

[10] H. Feng, G. Wang, W. Jin, X. Zhang, Y. Huang, A. Gao, H. Wu, G. Wu, P.K. Chu, Systematic study of inherent antibacterial properties of magnesium-based biomaterials, ACS Appl. Mater. Inter. 8 (2016) 9662–9673, https://doi.org/10.1021/acsami.6b02241.

[11] Z. Lin, S. Wu, X. Liu, S. Qian, P.K. Chu, Y. Zheng, K.M.C. Cheung, Y. Zhao, K.W. K. Yeung, A surface-engineered multifunctional TiO_2 based nano-layer simultaneously elevates the corrosion resistance, osteoconductivity and antimicrobial property of a magnesium alloy, Acta Biomater. 99 (2019) 495–513, https://doi.org/10.1016/j.actbio.2019.09.008.

[12] G. He, Y. Wu, Y. Zhang, Y. Zhu, Y. Liu, N. Li, M. Li, G. Zheng, B. He, Q. Yin, Y. Zheng, C. Mao, Addition of Zn to the ternary Mg-Ca-Sr alloys significantly improves their antibacterial property, J. Mater. Chem. B 3 (2015) 6676–6689, https://doi.org/10.1039/C5TB01319D.

[13] Y. Zhao, M.I. Jamesh, W.K. Li, G. Wu, C. Wang, Y. Zheng, K.W.K. Yeung, P.K. Chu, Enhanced antimicrobial properties, cytocompatibility, and corrosion resistance of plasma-modified biodegradable magnesium alloys, Acta Biomater. 10 (2014) 544–556, https://doi.org/10.1016/j.actbio.2013.10.012.

[14] E.K. Brooks, R. Ahn, M.E. Tobias, L.A. Hansen, N.R. Luke-Marshall, L. Wild, A. A. Campagnari, M.T. Ehrensberger, Magnesium alloy AZ91 exhibits antimicrobial properties *in vitro* but not *in vivo*, J. Biomed. Mater. Res. B Appl. Biomater. 106 (2018) 221–227, https://doi.org/10.1002/jbm.b.33839.

[15] A.V. Rudakova, A.V. Emeline, K.M. Bulanin, L.V. Chistyakova, M.V. Maevskaya, D. W. Bahnemann, Self-cleaning properties of zirconium dioxide thin films, J. Photochem. Photobiol. A 367 (2018) 397–405, https://doi.org/10.1016/j.jphotochem.2018.08.037.

[16] A. Moghanian, M. Zohourfazeli, M.H.M. Tajer, The effect of zirconium content on *in vitro* bioactivity, biological behavior and antibacterial activity of sol-gel derived 58S bioactive glass, J. Non-Cryst. Solids 546 (2020), 120262, https://doi.org/10.1016/j.jnoncrysol.2020.120262.

[17] A. Apratim, P. Eachempati, K.K. Krishnappa Salian, V. Singh, S. Chhabra, S. Shah, Zirconia in dental implantology: a review, J. Int. Soc. Prev. Community Dent. 5 (2015) 147–156, https://doi.org/10.4103/2231-0762.158014.

[18] D.S. Nakonieczny, A. Ziębowicz, Z.K. Paszenda, C. Krawczyk, Trends and perspectives in modification of zirconium oxide for a dental prosthetic applications – a review, Biocybern. Biomed. Eng. 37 (2017) 229–245, https://doi.org/10.1016/j.bbe.2016.10.005.

[19] E.D. de Avila, R.S. de Molon, B.P. Lima, R. Lux, W. Shi, M.J. Junior, D. M. Spolidorio, C.E. Vergani, F. de Assis Mollo Junior, Impact of physical chemical characteristics of abutment implant surfaces on bacteria adhesion, J. Oral Implantol. 42 (2016) 153–158, https://doi.org/10.1563/aaid-joi-D-14-00318.

[20] Z. Lin, Y. Zhao, P.K. Chu, L. Wang, H. Pan, Y. Zheng, S. Wu, X. Liu, K.M.C. Cheung, T. Wong, K.W.K. Yeung, A functionalized TiO_2/Mg_2TiO_4 nano-layer on biodegradable magnesium implant enables superior bone-implant integration and bacterial disinfection, Biomaterials 219 (2019) 119372, https://doi.org/10.1016/j.biomaterials.2019.119372.

[21] ISO 10993–5:2009 Biological Evaluation of Medical Devices - Part 5: Tests for *in Vitro* Cytotoxicity, 2009.

[22] S. Wang, K. Liu, X. Yao, L. Jiang, Bioinspired surfaces with superwettability: new insight on theory, design, and applications, Chem. Rev. 115 (2015) 8230–8293, https://doi.org/10.1021/cr400083y.

[23] K. Müller, D. Torres, J.B. Park, P. Liu, D. Stacchiola, D.E. Starr, NiO-MgO and CoO-MgO thin-film solid oxide solutions on a Mo(100) support: formation, reduction, and influence of the support, J. Phys. Chem. C 117 (2012) 280–287, https://doi.org/10.1021/jp308955n.

[24] M.-C. Zhao, P. Schmutz, S. Brunner, M. Liu, G.-l. Song, A. Atrens, An exploratory study of the corrosion of Mg alloys during interrupted salt spray testing, Corros. Sci. 51 (2009) 1277–1292, https://doi.org/10.1016/j.corsci.2009.03.014.

[25] C. Ubeda, G. Garces, P. Adeva, I. Llorente, G.S. Frankel, S. Fajardo, The role of the beta-$Mg_{17}Al_{12}$ phase on the anomalous hydrogen evolution and anodic dissolution of AZ magnesium alloys, Corros. Sci. 165 (2020), 108384, https://doi.org/10.1016/j.corsci.2019.108384.

[26] G. Wu, X. Zhang, Y. Zhao, J.M. Ibrahim, G. Yuan, P.K. Chu, Plasma modified Mg–Nd–Zn–Zr alloy with enhanced surface corrosion resistance, Corros. Sci. 78 (2014) 121–129, https://doi.org/10.1016/j.corsci.2013.09.007.

[27] M. Ascencio, M. Pekguleryuz, S. Omanovic, An investigation of the corrosion mechanisms of WE43 Mg alloy in a modified simulated body fluid solution: the effect of electrolyte renewal, Corros. Sci. 91 (2015) 297–310, https://doi.org/10.1016/j.corsci.2014.11.034.

[28] M.I. Jamesh, G. Wu, Y. Zhao, D.R. McKenzie, M.M.M. Bilek, P.K. Chu, Electrochemical corrosion behavior of biodegradable Mg–Y–RE and Mg–Zn–Zr alloys in Ringer's solution and simulated body fluid, Corros. Sci. 91 (2015) 160–184, https://doi.org/10.1016/j.corsci.2014.11.015.

[29] J.J. Zhuang, Y.Q. Guo, N. Xiang, Y. Xiong, Q. Hu, R.G. Song, A study on microstructure and corrosion resistance of ZrO_2-containing PEO coatings formed on AZ31 Mg alloy in phosphate-based electrolyte, Appl. Surf. Sci. 357 (2015) 1463–1471, https://doi.org/10.1016/j.apsusc.2015.10.025.

[30] W. Jin, G. Wu, H. Feng, W. Wang, X. Zhang, P.K. Chu, Improvement of corrosion resistance and biocompatibility of rare-earth WE43 magnesium alloy by neodymium self-ion implantation, Corros. Sci. 94 (2015) 142–155, https://doi.org/10.1016/j.corsci.2015.01.049.

[31] R. Walter, M.B. Kannan, Influence of surface roughness on the corrosion behaviour of magnesium alloy, Mater. Des. 32 (2011) 2350–2354, https://doi.org/10.1016/j.matdes.2010.12.016.

[32] B. Yoo, K.R. Shin, D.Y. Hwang, D.H. Lee, D.H. Shin, Effect of surface roughness on leakage current and corrosion resistance of oxide layer on AZ91 Mg alloy prepared by plasma electrolytic oxidation, Appl. Surf. Sci. 256 (2010) 6667–6672, https://doi.org/10.1016/j.apsusc.2010.04.067.

[33] J. Wang, V. Giridharan, V. Shanov, Z. Xu, B. Collins, L. White, Y. Jang, J. Sankar, N. Huang, Y. Yun, Flow-induced corrosion behavior of absorbable magnesium-based stents, Acta Biomater. 10 (2014) 5213–5223, https://doi.org/10.1016/j.actbio.2014.08.034.

[34] C.H. Pan, Z.B. Zhou, X.W. Yu, Coatings as the useful drug delivery system for the prevention of implant-related infections, J. Orthop. Surg. Res. 13 (2018) 11, https://doi.org/10.1186/s13018-018-0930-y.

[35] R.M. Donlan, J.W. Costerton, Biofilms: survival mechanisms of clinically relevant microorganisms, Clin. Microbiol. Rev. 15 (2002) 167–193, https://doi.org/10.1128/cmr.15.2.167-193.2002.

[36] T. Wei, Q. Yu, H. Chen, Responsive and synergistic antibacterial coatings: fighting against bacteria in a smart and effective way, Adv. Healthc. Mater. 8 (2019) 24, https://doi.org/10.1002/adhm.201801381.

[37] A.S.D. Al-Radha, D. Dymock, C. Younes, D. O'Sullivan, Surface properties of titanium and zirconia dental implant materials and their effect on bacterial adhesion, J. Dent. 40 (2012) 146–153, https://doi.org/10.1016/j.jdent.2011.12.006.

[38] P.F. Manicone, P.R. Iommetti, L. Raffaelli, An overview of zirconia ceramics: basic properties and clinical applications, J. Dent. 35 (2007) 819–826, https://doi.org/10.1016/j.jdent.2007.07.008.

[39] E.D. de Avila, M.J. Avila-Campos, C.E. Vergani, D.M.P. Spolidorio, F.D. Mollo, Structural and quantitative analysis of a mature anaerobic biofilm on different implant abutment surfaces, J. Prosthet. Dent. 115 (2016) 428–436, https://doi.org/10.1016/j.prosdent.2015.09.016.

[40] J. Li, S. Qian, C. Ning, X. Liu, rBMSC and bacterial responses to isoelastic carbon fiber-reinforced poly(ether-ether-ketone) modified by zirconium implantation, J. Mater. Chem. B 4 (2016) 96–104, https://doi.org/10.1039/c5tb01784j.

[41] Y. Lv, W. Yao, R. Zong, Y. Zhu, Fabrication of wide-range-visible photocatalyst Bi_2WO_{6-x} nanoplates via surface oxygen vacancies, Sci. Rep. 6 (2016) 19347, https://doi.org/10.1038/srep19347.

[42] Y. Lu, Y. Huang, Y. Zhang, J.j. Cao, H. Li, C. Bian, S.C. Lee, Oxygen vacancy engineering of $Bi_2O_3/Bi_2O_2CO_3$ heterojunctions: implications of the interfacial charge transfer, NO adsorption and removal, Appl. Catal. B Environ. 231 (2018) 357–367, https://doi.org/10.1016/j.apcatb.2018.01.008.

[43] L. Renuka, K.S. Anantharaju, S.C. Sharma, H.P. Nagaswarupa, S.C. Prashantha, H. Nagabhushana, Y.S. Vidya, Hollow microspheres Mg-doped ZrO_2 nanoparticles: Green assisted synthesis and applications in photocatalysis and photoluminescence, J. Alloys Compd. 672 (2016) 609–622, https://doi.org/10.1016/j.jallcom.2016.02.124.

[44] J. Wang, Z. Wang, B. Huang, Y. Ma, Y. Liu, X. Qin, X. Zhang, Y. Dai, Oxygen vacancy induced band-gap narrowing and enhanced visible light photocatalytic activity of ZnO, ACS Appl. Mater. Interf. 4 (2012) 4024–4030, https://doi.org/10.1021/am300835p.

[45] X. Wu, S. Yin, Q. Dong, C. Guo, H. Li, T. Kimura, T. Sato, Synthesis of high visible light active carbon doped TiO_2 photocatalyst by a facile calcination assisted solvothermal method, Appl. Catal. B Environ. 142–143 (2013) 450–457, https://doi.org/10.1016/j.apcatb.2013.05.052.

[46] M. Xing, J. Zhang, F. Chen, B. Tian, An economic method to prepare vacuum activated photocatalysts with high photo-activities and photosensitivities, Chem. Commun. 47 (2011) 4947–4949, https://doi.org/10.1039/c1cc10537j.

[47] H. Liu, F. Zeng, Y. Lin, G. Wang, F. Pan, Correlation of oxygen vacancy variations to band gap changes in epitaxial ZnO thin films, Appl. Phys. Lett. 102 (2013) 181908, https://doi.org/10.1063/1.4804613.

[48] H. Li, J. Shi, K. Zhao, L. Zhang, Sustainable molecular oxygen activation with oxygen vacancies on the {001} facets of BiOCl nanosheets under solar light, Nanoscale 6 (2014) 14168–14173, https://doi.org/10.1039/c4nr04810e.

[49] D. Cui, L. Wang, K. Xu, L. Ren, L. Wang, Y. Yu, Y. Du, W. Hao, Band-gap engineering of BiOCl with oxygen vacancies for efficient photooxidation properties under visible-light irradiation, J. Mater. Chem. 6 (2018) 2193–2199, https://doi.org/10.1039/c7ta09897a.

[50] V. Lakshmi Prasanna, R. Vijayaraghavan, Insight into the mechanism of antibacterial activity of ZnO: surface defects mediated reactive oxygen species even in the dark, Langmuir 31 (2015) 9155–9162, https://doi.org/10.1021/acs.langmuir.5b02266.

[51] C. Zhu, C. Li, M. Zheng, J.J. Delaunay, Plasma-induced oxygen vacancies in ultrathin hematite nanoflakes promoting photoelectrochemical water oxidation, ACS Appl. Mater. Interf. 7 (2015) 22355–22363, https://doi.org/10.1021/acsami.5b06131.

[52] Y.J. Hao, B. Liu, L.G. Tian, F.T. Li, J. Ren, S.J. Liu, Y. Liu, J. Zhao, X.J. Wang, Synthesis of {111} facet-exposed MgO with surface oxygen vacancies for reactive oxygen species generation in the dark, ACS Appl. Mater. Interf. 9 (2017) 12687–12693, https://doi.org/10.1021/acsami.6b16856.

[53] W. Chang, D.A. Small, F. Toghrol, W.E. Bentley, Global transcriptome analysis of *Staphylococcus aureus* response to hydrogen peroxide, J. Bacteriol. 188 (2006) 1648–1659, https://doi.org/10.1128/JB.188.4.1648-1659.2006.

[54] A.A. Glynn, S.T. O'Donnell, D.C. Molony, E. Sheehan, D.J. McCormack, J. P. O'Gara, Hydrogen peroxide induced repression of *icaADBC* transcription and biofilm development in *Staphylococcus epidermidis*, J. Orthop. Res. 27 (2009) 627–630, https://doi.org/10.1002/jor.20758.

[55] D. Cue, M.G. Lei, C.Y. Lee, Genetic regulation of the intercellular adhesion locus in staphylococci, Front Cell Infect. Microbiol. 2 (2012) 38, https://doi.org/10.3389/fcimb.2012.00038.

[56] Y. Li, L. Liu, P. Wan, Z. Zhai, Z. Mao, Z. Ouyang, D. Yu, Q. Sun, L. Tan, L. Ren, Z. Zhu, Y. Hao, X. Qu, K. Yang, K. Dai, Biodegradable Mg-Cu alloy implants with

antibacterial activity for the treatment of osteomyelitis: *In vitro* and *in vivo* evaluations, Biomaterials 106 (2016) 250–263, https://doi.org/10.1016/j.biomaterials.2016.08.031.

[57] F. Song, H. Koo, D. Ren, Effects of material properties on bacterial adhesion and biofilm formation, J. Dent. Res. 94 (2015) 1027–1034, https://doi.org/10.1177/0022034515587690.

[58] S. Wu, B. Zhang, Y. Liu, X. Suo, H. Li, Influence of surface topography on bacterial adhesion: a review (Review), Biointerphases 13 (2018), 060801, https://doi.org/10.1116/1.5054057.

[59] W. Teughels, N. Van Assche, I. Sliepen, M. Quirynen, Effect of material characteristics and/or surface topography on biofilm development, Clin. Oral Implants Res. 17 (Suppl 2) (2006) 68–81, https://doi.org/10.1111/j.1600-0501.2006.01353.x.